Quasi-10-day wave activity in the southern high-latitude MLT region and its relation to the large-scale instability and gravity wave drag

Wonseok Lee[1], In-Sun Song[1], Byeong-Gwon Song[1], Yong Ha Kim[2]

[1]Department of Atmospheric Sciences, Yonsei University, Seoul 03722, South Korea
[2]Department of Astronomy and Space Science, Chungnam National University, Daejeon 34134, South Korea

Correspondence to: In-Sun Song (songi@yonsei.ac.kr)

Abstract. Seasonal variation of westward-propagating quasi-10-day wave (Q10DW) in the mesosphere and lower thermosphere of the Southern Hemisphere (SH) high-latitude regions is investigated using meteor radar (MR) observations for the period of 2012–2016 and Specified Dynamics (SD) version of the Whole Atmosphere Community Climate Model (WACCM). The phase difference of meridional winds measured by two MRs located in Antarctica gives observational estimates of the amplitude and phase of Q10DW with zonal wavenumber 1 (W1). The amplitude of the observed Q10DW-W1 is large around equinoxes. In order to elucidate the variations of the observed Q10DW-W1 and its possible amplification mechanism, we carry out two SD-WACCM experiments nudged towards the MERRA-2 reanalysis from the surface up to ~60 km (EXP60) and ~75 km (EXP75). Results of the EXP75 indicate that the observed Q10DW-W1 can be amplified around the barotropic/baroclinic instability regions in the middle mesosphere around 60°S–70°S. In the EXP60, it is also found that Q10DW-W1 is amplified around the instability regions, but the amplitude is too large compared with MR observations. The large-scale instability in the EXP60 in the SH summer mesosphere is stronger than that in the EXP75 and Microwave Limb Sounder observation. The larger instability in the EXP60 is related to the large meridional and vertical variations of polar mesospheric zonal winds in association with gravity wave parameterization (GWP). Given uncertainties inherent in GWP, these results can suggest that it is possible for models to spuriously generate traveling planetary waves such as Q10DW, especially in summer, due to the excessively strong large-scale instability in the SH high-latitude mesosphere.

1. Introduction

A series of Rossby normal modes (free oscillations) is the homogeneous solution of the governing equations on a sphere linearized with respect to the isothermal and quiescent reference atmosphere (e.g., Andrews et al., 1987; Forbes et al., 1995; Salby, 1984). Traveling normal modes exhibit clear planetary-scale spatiotemporal oscillations throughout the whole atmosphere, and for sufficiently large amplitudes, these traveling planetary waves (PWs) can play an important role in the momentum and energy transfer to the mean flow (Salby, 1984). Three gravest traveling normal modes have been observed: Westward-propagating zonal-wavenumber-1 PWs with periods of approximately 5, 10, and 16 days. The classical wave theory based on the isothermal and quiescent atmosphere gives the theoretical periods of 5, 8.3, and 12.5 day, but the periods in the real atmosphere can be shifted to values close to 5, 10, and 16 days, respectively (Salby, 1981a, b), due to influences of the vertical and meridional variation of the mean horizontal winds and temperature.

Among the gravest modes, the quasi-5-day wave (Q5DW) and quasi-16-day wave (Q16DW) have extensively been studied through observations, modeling, and assimilation products: Ground-based observations (e.g., Day and Mitchell, 2010; He et al., 2020b; Mitra et al., 2022), satellite observations (e.g., Forbes and Zhang, 2017; Huang et al., 2022), reanalysis data (e.g., Huang et al., 2017), and simulations (e.g., Qin et al., 2021). Using meteor radars (MRs) located in the northern and southern polar regions, Day and Mitchell (2010) showed that PW activity is strong during winter and the seasonal variation of PW is similar in both polar regions. According to Qin et al. (2021) and Mitra et al. (2022), the barotropic and baroclinic instabilities are the possible sources of Q5DW and Q16DW in that the waves can draw energy from the mean flow in the instability region. The disturbance of zonal-mean flow frequently occurs during the large-scale meteorological events such as sudden stratospheric warming (SSW). It has been reported that the amplitude of Q5DW or Q16DW increases during SSW events (Eswaraiah et al., 2016; Lee et al., 2021; Li et al., 2021; Ma et al., 2022). In addition, the amplified PWs can interact with tidal waves through the in-situ nonlinear interaction, resulting ionospheric disturbances during SSW (e.g., Goncharenko et al., 2020; Forbes et al., 2021; Liu et al., 2021; Qin et al., 2019).

In contrast, the westward propagating quasi-10-day wave (Q10DW) with zonal wavenumber 1 (W1) has received little attention compared to the other gravest normal modes. Forbes and Zhang (2015) showed that Q10DW-W1 has a mean period of 9.8 ± 0.4 days using the temperature measurements from the Sounding of the Atmosphere using Broadband Emission Radiometry (SABER) instrument mounted on NASA's TIMED (Thermosphere Ionosphere Mesosphere Energetics Dynamics) satellite in 2002–2013. They presented that the large amplitude of Q10DW-W1 is found in the mid-latitude (40–50° latitude) mesosphere and lower thermosphere (MLT) region of both hemispheres in equinoxes, although their results are limited to the latitude of 50° because of the yaw cycle of the satellite. Hirooka (2000) reported that the global structure of Q10DW-W1 using the Improved Stratosphere and Mesospheric Souder (ISAMS) instrument aboard Upper Atmosphere Research Satellite (UARS) from November 1991 to May 1992. The results also showed that the Q10DW-W1 is active during equinoxes and winter at 0.1 hPa (~65 km). In addition, it is found that nonuniform and background zonal wind field can influence the structure of the wave in the mesosphere. The amplitude of the Q10DW-W1 is uniform or decays in the vertical near the mesopause, and it does not increase above the mesosphere, even though the critical layer is absent. Using the airglow intensities simulated by the global circulation model assimilated by the reanalysis data from ground to 30 km, Egito et al. (2017) also found that the 10-day oscillation is dominant from autumn to spring in the mid-latitude MLT region. More recently, Huang et al. (2021) investigated the Q10DW activity based on the Modern-Era Retrospective analysis for Research and Applications version 2 (MERRA-2) reanalysis data. They showed that the dominant components of Q10DW are westward-propagating waves with zonal wavenumber 1 during winter and spring in the stratosphere and mesosphere and eastward-propagating waves with zonal wavenumber 1 and 2, which are excited in the mesospheric instability region. Although both westward and eastward Q10DW modes are found, they mainly focus on the eastward propagating Q10DW.

Several studies have investigated the response of Q10DW-W1 to SSWs. Matthias et al. (2012) conducted a composite analysis of wave activities during major Northern Hemisphere (NH) SSWs from 1989 to 1998, revealing an amplification of Q10DW-W1 in the NH high-latitude MLT region following major SSW events. He et al. (2020a, 2020b) utilized NH MRs to observe the occurrence of Q10DW-W1 and Q16DW-W1 during four winter major SSWs. They found that these waves persisted for approximately three to five whole cycles during the events. Chandran et al. (2013) examined the forcing of secondary PWs-W1 driven by stratospheric instability on zonal winds as a response to 2012 NH minor SSW. Sassi and Liu (2014) conducted numerical simulations during minor and major NH SSWs and solar minimum condition. They found that PWs-W1 with periods between 2 and 10 days originating in the high-latitude NH could propagate equatorward and influence equatorially trapped tides. This equatorward propagation of secondary PWs was also reported by Qin et al. (2022). They suggested that secondary PWs-W1 with periods of 10 to 16 days generated in the high-latitude NH during sudden stratospheric final warming could impact the Southern Hemisphere (SH) stratosphere, depending on the phase of Quasi-Biennial Oscillation (QBO). In the SH, studies by Lee et al. (2021) and Wang et al. (2021) using SH MRs reported that Q10DW was amplified prior to 2019 SH SSW. Yamazaki and Matthias (2019) reported that the Q10DW-W1 is not only intensified during SSWs but also affected by seasonal timing of SSWs (i.e., final stratospheric warming) in stratospheric instability regions.

While the amplification mechanism of Q10DW-W1 generated following SSWs has been addressed in previous studies (e.g., Qin et al., 2022, Yin et al., 2023), the specific mechanisms driving their seasonal amplification during equinoxes remain less explored. In the present study, we focus on the seasonal variation of Q10DW-W1 in the SH high-latitude MLT region using MRs located in Antarctica. Plus, we carry out numerical simulations using the Specified Dynamics version of the Whole Atmosphere Community Climate Model (SD-WACCM) nudged towards MERRA-2 reanalysis data in order to elucidate the observed Q10DW-W1 and its amplification mechanism. Section 2 describes two MRs located in the Davis station (68.6°S, 77.9°E) and King Sejong Station (KSS; 62.2°S, 58.8°W) and how we obtain Q10DW-W1 from the observations. Also, the SD-WACCM experiments and Microwave Limb Sounder (MLS) data used for validation are described in Section 2. Results are presented in Section 3. In Section 3.1, we show seasonal variation of observed and modeled Q10DW-W1 in the SH high-latitude MLT region. The amplification mechanism of Q10DW is discussed in Section 3.2. Q10DW activities from SD-WACCM simulations are demonstrated in Section 3.3. In Section 4, the results are summarized, and their implications are discussed.

2. Data and Method

2.1 Meteor Radars

In this study, we use two MRs located in the Davis station (68.6°S, 77.9°E) and King Sejong Station (KSS; 62.2°S, 58.8°W), Antarctica from 2012 to 2016. The operating frequencies of both Davis and KSS MRs are 33.2 MHz and the peak powers are 6.8 kW and 12 kW, respectively. Details of the operation parameters of Davis and KSS are summarized in Holdsworth et al. (2008) and Lee et al. (2018), respectively. A large number of studies has been performed to investigate the PW or tidal activities in the MLT region with a single-station measurements of horizontal winds from an MR (e.g., Eswaraiah et al., 2019; Luo et al., 2021; Wang et al., 2021; Liu et al., 2022; Lee et al., 2021). However, single-station analysis has a limitation in diagnosing the wave propagation direction, and thus most of such studies focused on the timing of occurrence and amplitude variations of wave with a particular periodicity. For detailed analysis of PWs based on the Rossby normal modes, propagation directions and wavenumbers need to be considered. Recently, He et al. (2018) developed a method of estimating wave propagation direction and wavenumber as well as amplitude by adopting Phase Differencing Technique (PDT) to longitudinally separated MR observations based on the method of Walker et al. (2004). Since the longitude difference (λ_Δ) between Davis and KSS is about 137°, it is appropriate for analyzing PWs with zonal wavenumber 1 by applying the PDT. In order to estimate the zonal wavenumber (s), we first make a continuous wavelet transform from the daily-mean Davis and KSS MRs data ($W_{(f,t)}^{Davis}$, $W_{(f,t)}^{KSS}$), respectively, using the Morlet wavelet function as a mother wavelet function (Torrence and Compo, 1998). Then, the cross wavelet spectrum $C_{(f,t)}$ is derived: $C_{(f,t)} = W_{(f,t)}^{*Davis} W_{(f,t)}^{KSS}$, where * denotes the complex conjugate. Using the phase difference (θ_Δ) obtained from $\theta_\Delta = \mathrm{Arg}(C_{(f,t)})$ at a given frequency and time, we estimate zonal wavenumber (s): $s = (-\theta_\Delta/(2\pi) + C)/\lambda_\Delta$. In this study, we focus on the PW activity with s = 1, and the number of whole wave cycle (C) between two stations is set to be zero (see He et al., 2018 for detailed PDT analysis).

Classical wave theory shows that the latitudinal structures of zonal and meridional wind components for Q10DW normal mode from the Laplace tidal equation are antisymmetric and symmetric with respect to the equator, respectively (e.g., Figure 1 in Yamazaki and Matthias, 2019). The magnitude of Q10DW-W1 has maxima at the latitude of 25° and poles for zonal and meridional wind components, respectively. Around the latitude of 65°S close to the latitudes of the two MR observation sites, the normalized amplitude of Q10DW-W1 normal mode for the zonal wind is nearly zero, but the normalized normal mode magnitude for the meridional wind is larger than the half of the maximum magnitude for the meridional wind (Yamazaki and Matthias, 2019). For this reason, daily-mean meridional wind data from the MRs is used for the Q10DW analysis.

2.2 SD-WACCM

In this study, for detailed analysis of the observed Q10DW-W1 activity and its amplification mechanism, we compare observational results with Q10DW-W1 simulated using the Specified Dynamics (SD) version of WACCM version 4 (Marsh et al., 2013). WACCM4 is a high-top (up to the lower thermosphere about 140 km) atmospheric component model of the Community Earth System Model developed at the National Center for Atmospheric Research. WACCM4 employs Community Atmospheric Model (CAM) version 4 physics package. The default horizontal resolution of WACCM4 is $1.9°\times2.5°$ (lat. × long.), and it uses the 88 hybrid sigma vertical levels for the SD mode. Since we focus on the PWs such as Q10DW-W1, daily-mean values from the SD-WACCM are used. In this study, two SD-WACCM experiments with two different nudging depths (EXP60 and EXP75) are performed. In the EXP60 and EXP75, model variables are nudged towards the MERRA-2 reanalysis data from surface to about 60 km in altitude and 75 km, respectively. The MERRA-2 reanalysis is produced by assimilating various types of observations into the Goddard Earth Observing System version 6 (GEOS-6) global model (Gelaro et al., 2017). In addition to conventional meteorological observations and operational satellite measurements, the Earth Observing System (EOS) Aura MLS temperature and ozone data are included in the assimilation procedure of the MERRA-2 from 5 hPa (~37 km) up to 0.02 hPa (~75 km) and from 250 hPa (~10 km) to 0.1 hPa (~65 km), respectively (Gelaro et al., 2017; McCormack et al., 2021). There is a divergence damping layer near the top boundary of the GEOS-6 model used for production of the MERRA-2 reanalysis (Fujiwara et al., 2017). The divergence damping is often used to effectively and selectively remove high-frequency (noisy) gravity waves keeping the large-scale circulation and PWs structure less changed (Jablonowski and Williamson, 2011). As a result, MERRA-2 reanalysis can reflect the large-scale MLT variabilities (e.g., McCormack et al., 2021; Harvey et al., 2021). As suggested by Brakebusch et al.

(2013), nudging coefficients for EXP60 and EXP75 are 0.01 s^{-1} below the altitudes of 50 km and 65 km, respectively, and they linearly decrease and become zero above the altitudes of 60 km and 75 km, respectively.

WACCM simulation requires the data of sea surface temperature, sea ice fraction, solar and geomagnetic indices, and ionization rate by energetic particle precipitation (EPP) for the time period of simulations. The sea surface temperature and sea ice fraction data are produced by the NOAA Optimum Interpolation (Reynolds et al., 2002). The solar and geomagnetic indices are obtained from NASA GSFC/SPDF OMNIWeb interface (https://omniweb.gsfc.nasa.gov/ow.html). The EPP ionization rate is provided by the CCMI reference-C2 data for the period of 1960–2100 (Eyring et al., 2013). Regarding MLT dynamics, effects of gravity wave drag (GWD) are crucial. WACCM includes a suite of GWD parameterizations (Richter et al., 2010) for effects of unresolved GW momentum transfer from orography (McFarlane, 1987), deep convection (Beres et al., 2005), and frontal activity (Charron and Manzini, 2002). SD-WACCM simulations start from January 1, 2011 and end at the end of 2016. First one-year results are discarded as a spin-up, and results for 2012–2016 are compared with MR observations.

2.3 MLS

For validation of Q10DW-W1 estimates obtained from MR observations, we derive the geostrophic winds from geopotential height (GPH) data (version 5.1 product) measured using MLS onboard the NASA's EOS Aura satellite (Schwartz et al., 2008). Geostrophic wind components are computed following Matthias and Ern (2018). The

Aura satellite launched on July 2004 is in a sun-synchronous orbit with an altitude of 705 km. Spatial coverage of MLS instrument is from 82°S to 82°N with a 165 km resolution along the track. The sun-synchronous orbit of Aura satellite can provide a global coverage data per day with about 15 orbits. The global coverage of GPH is produced using daily mean values in 5°×5° (lat. × long.) grids. In this process, GPH data is filtered on the basis of the recommended precision, status, quality, and convergence thresholds of Version 5.0 Level 2 and 3 data quality and description document (https://mls.jpl.nasa.gov/data/v5-0_data_quality_document.pdf).

3. Results and Discussion

3.1 Seasonal variation of Q10DW-W1 in the MLT region

The perturbation meridional wind for Q10DW-W1 is symmetric in latitude about the equator as mentioned earlier. Therefore, in order to extract and analyze Q10DW-W1, which is potentially related to the Rossby normal mode in the MLT region, it is necessary to confirm whether the latitudinal structure of Q10DW-W1 has the hemispheric symmetry. Although the KSS and Davis MR observations can provide information about the longitudinal propagation of Q10DW-W1, it is impossible to estimate the latitudinal structure using these radars alone. In this study, the meridional geostrophic winds obtained from the MLS geopotential data are used to confirm the hemispheric symmetry of Q10DW-W1 estimated from MRs. The amplitudes of Q10DW-W1 in the MLS are obtained using the two-dimensional Fast Fourier transform (FFT) of the geostrophic meridional winds averaged over the height range of 80–90 km in time (30-day sliding window) and longitude domain. The time-latitude cross section of the amplitude of Q10DW-W1 derived from the MLS geostrophic meridional wind averaged over the height range of 80–90 km is presented in the Supplement (Fig. S1). Hereafter, the Q10DW denotes westward-propagating quasi-10-day normal mode wave with zonal wavenumber 1 and the hemispheric symmetry, where quasi-10-day periodicity means the periods between 9 and 11 days. Unless the hemispheric symmetry is satisfied, the analyzed westward propagating signals with zonal wavenumber 1 are referred to as quasi-10-day-like oscillations (Q10DOs).

Figure 1 shows the time-height distributions of the amplitudes of Q10DWs and Q10DOs derived from the daily-mean meridional winds observed at the Davis and KSS MRs using the PDT method. The regions shaded in gray represent the time periods when the hemispheric symmetry is not found in the MLS results as shown in Fig. S1. The time periods of the hemispheric symmetries are defined by the periods when the amplitudes of the MLS meridional geostrophic winds (vertically averaged over 80–90 km) with quasi-10-day periodicity exceed 3.5 m s^{-1} in both 60°N–80°N and 60°S–80°S. The MLS results in solstices are generally shaded in gray (see Fig. S1). This result indicates that Q10DWs in a form of normal modes are found during equinoxes, which is consistent with the results from Forbes and Zhang (2015). Using the periods of the hemispheric symmetry of the Q10DW obtained from the MLS, we identify the normal mode Q10DW from the Davis and KSS MR observations.

The 5-yr average (The bottom-most panel of Fig. 1) between 2012 and 2016 indicates that the Q10DWs are generally enhanced from late February to April and from late August to September in the altitude range of 82–98 km with the maximum amplitude of 2.6 m s^{-1}. The Q10DWs are usually more amplified in early spring from late August to September with the largest amplitudes around the altitudes of 90–95 km.

Large amplitudes are found in winter (July to mid-August), but they are unlikely to represent the normal mode Q10DWs, as it is clear from the gray shading in winter. According to Wang et al. (2021), the nonlinear wave-wave interaction can generate Q10DOs in southern winter. Their Q10DOs are eastward propagating, interacting with stationary PWs with zonal wavenumber 1. Meanwhile, the Q10DWs and Q10DOs (Fig. 1) obtained from two MRs using the PDT method are westward propagating. Understanding of the mechanisms of the winter-time westward-propagating Q10DOs is beyond the scope of this study, and it requires continuing researches. It is important to note that the amplitudes of Q10DW are systematically lower in MRs compared to the MLS results. These discrepancies might be attributed to the accuracy of estimated geostrophic winds from the MLS data, or the inherent limitations of MR analysis, which in our case involves only two stations located at slightly different latitudes.

For individual years, it is also found that the amplitude of Q10DW is generally large in equinoxes (see panels for each year in Figs. 1 and S1). During March–April (autumn), active Q10DWs are identified, and their amplitudes reach up to ~3 m s^{-1} in 2014 and 2015. Particularly, the peak in September (spring) is prominent in 2016. These MR observation results are remarkably consistent with results obtained using satellite geopotential height in the SH high-latitude region (Forbes and Zhang, 2015). Occasionally, large amplitude Q10DWs are observed near the altitude of 98–100 km in equinoxes (e.g., April 2015), but results around 100 km can be less reliable because the number of MR echoes above 96 km is much smaller than that around 90 km (Lee et al., 2022).

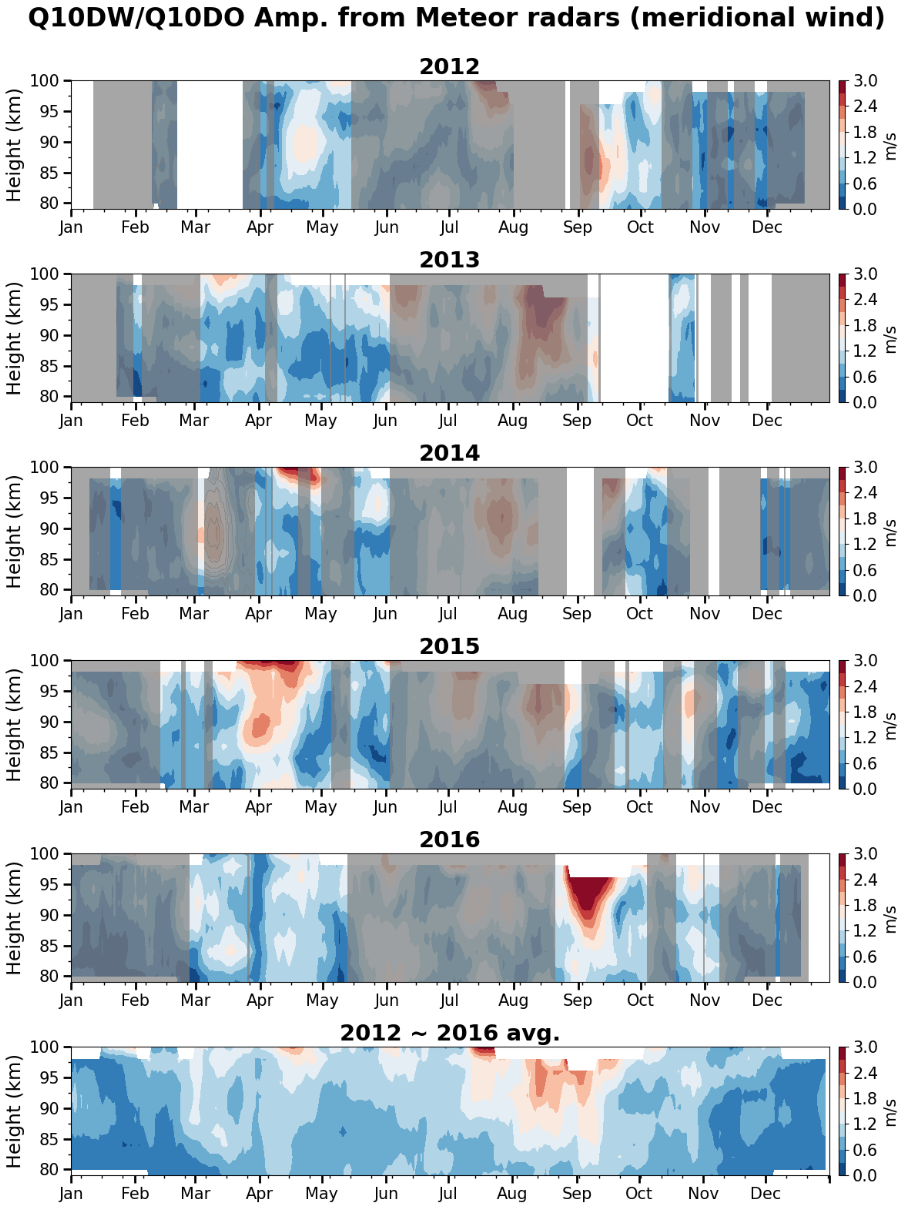

Figure 1. Time-height distributions of the amplitudes of Q10DWs (unshaded region) and Q10DOs (shaded region) derived from meridional winds observed by MRs at Davis (68.6°S, 77.9°E) and KSS (62.2°S, 58.8°W) for 2012–2016. The bottom-most panel shows the 5-yr average from 2012 to 2016. The gray shading represents time periods where the hemispheric symmetry is unclear in the MLS results (see the text for details of the unclearness of symmetry).

Figure 2 demonstrates the time-height distributions of the amplitudes of Q10DWs and Q10DOs around the latitude of 63°S in the EXP75 SD-WACCM simulation for the altitude range of 60–110 km for 2012–2016, along with the hemispheric symmetry period obtained from the MLS results. The bottom-most panel of Fig. 2 shows the 5-yr average from 2012 to 2016. The amplitudes are obtained by decomposing the meridional winds obtained from the simulation into westward propagating Fourier modes with zonal wavenumber 1 using the 2D FFT in time (30-day sliding window) and longitude domain around 63°S. From Fig. 2, it is clear that the seasonal variations of Q10DW amplitudes obtained from the simulation have year-to-year variations, as in the Q10DW amplitudes derived from the two MRs. However, the Q10DW activities observed from the MR observations are much smaller than those in the EXP75 simulation (see Fig. 1).

The 5-yr average in Fig. 2 shows that there are four main time periods (February, April, September, November) when the modeled Q10DWs and Q10DOs are active in the EXP75. The time periods of April and September are consistent with the MR observations in terms of Q10DW amplitudes and the hemispheric symmetry obtained from the MLS, but the other periods are not. The active signals simulated in February and November do not appear to be normal mode Q10DWs because the hemispheric symmetry is not seen in the MLS data during February and November. For a more comprehensive understanding of the Q10DOs in the EXP75 during February and November, we will discuss in more detail later in Section 3.3 by comparing between the EXP75 and EXP60.

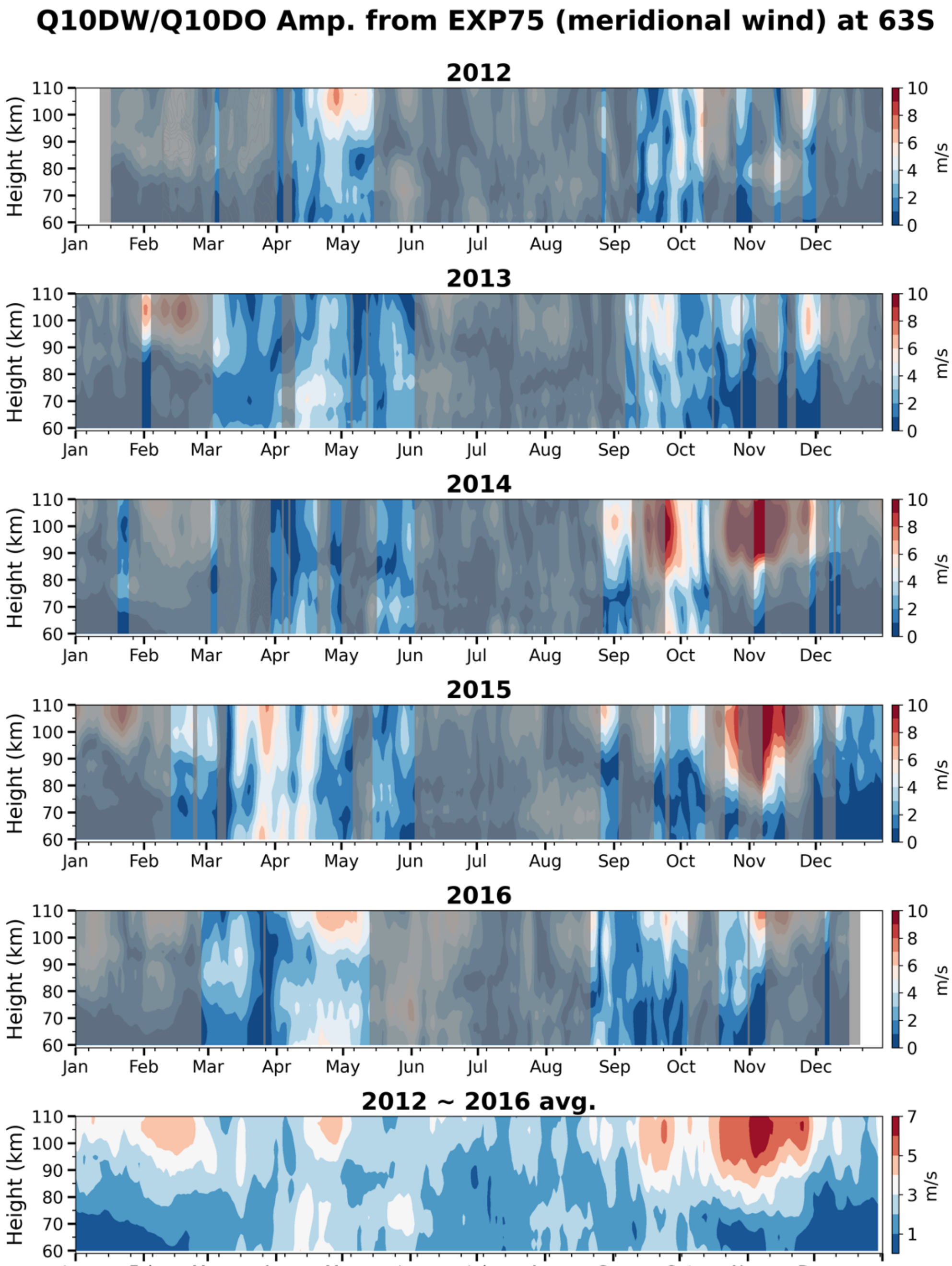

Figure 2. Time-height distributions of the amplitudes of Q10DWs (unshaded region) and Q10DOs (shaded region) around 63°S for 2012–2016 in the EXP75. The bottom-most panel shows the 5-yr average between 2012 and 2016. The gray shaded areas represent periods where the hemispheric symmetry is not observed in the MLS results.

Figure 3 shows time series of the normalized amplitudes of Q10DWs and Q10DOs obtained from the MR observations (black) and EXP75 simulation (blue). Normalization is carried out by averaging the amplitudes in the altitude range between 80 and 100 km and dividing the 5-yr averaged values by the respective maximum values in the same altitude range. We select the dates when (i) the amplitudes obtained from both MRs and EXP75 exceed their respective 5-yr mean values, (ii) their correlation is relatively large (> 0.6), and (iii) the hemispheric symmetry occurs in the MLS results. The correlation coefficients are computed for sliding 7-day windows with 1-day step. The dates when the three criteria are satisfied are represented by yellow boxes on abscissa in Fig. 3. The total number of the dates when the Q10DW was substantially active in both observations and model (EXP75) is 46. Using EXP75 results on the selected dates, the amplification mechanisms of the observed Q10DW will be discussed.

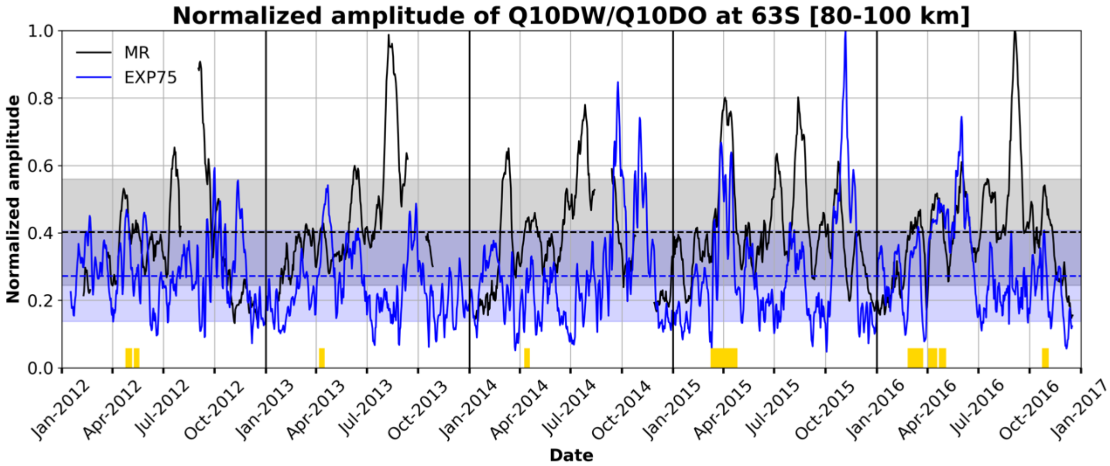

Figure 3. Time series of normalized amplitudes of Q10DW/Q10DOs from the observations (black line) and EXP75 simulation (blue line). The dashed lines and shaded areas represent the mean and standard deviation of normalized amplitude of Q10DW/Q10DOs from the observations (black) and EXP75 (blue), respectively. Yellow boxes on abscissa indicate the dates when the normalized amplitudes from both MRs and EXP75 can be considered to be due to the normal mode Q10DWs.

3.2 Amplification mechanisms of Q10DW

The amplitude of upward propagating PWs grows with height when their vertical propagation is allowed, but it can decrease with height in the evanescent region where the square of refractive index n^2 becomes negative. Regions of negative n^2 are often accompanied by regions of the negative latitudinal gradient of zonal-mean potential vorticity ($\bar{q}_\phi$), where $\bar{q}$ is the zonal-mean quasi-geostrophic potential vorticity (QGPV), the overbar denotes zonal averaging, ϕ is the latitude, and the subscript ϕ denotes the partial derivative in the latitudinal direction. In the regions of negative $\bar{q}_\phi$, the barotropic and baroclinic instabilities can occur (Matsuno, 1970), and it is known that PWs can amplify extracting energy from the mean flow while they pass through the instability regions (Meyer and Forbes, 1997; Cohen et al., 2013). If PWs somehow reach their critical lines within an instability region, it is possible for these PWs to tunnel through the critical lines (Rhodes et al., 2021). In case that the evanescent region is thin enough, and the PWs can reach their critical lines, it is also possible for the overreflection to take place, resulting in the amplified PWs and the propagation of the amplified PWs out of the overreflection region (Lindzen et al., 1980; Rhodes et al., 2021).

Another possible way of modulating PWs is their excitation by the nonconservative GW forcing (Song et al., 2020). Nonconservative GWD forcing (NCGWD; Z') can generate PWs as it is clearly seen from the perturbation QGPV equation given in the form of wave action conservation equation (1) when diabatic forcing is ignored in Z' [see Andrews et al. (1987) and Palmer (1982) for details]:

$$\frac{\partial A}{\partial t} + \boldsymbol{\nabla} \cdot \mathbf{F} = \rho_0 \overline{Z' q'_{(M)}} / (\bar{q}_\phi / a), \tag{1}$$

where a is the earth's mean radius; ρ_0 is the reference density given as an exponentially decreasing function of log-pressure height z; the prime denotes the perturbation from the respective zonal mean; A, defined below using $q'_{(M)}$, is the wave-activity density in the spherical QG system; $q'_{(M)}$ is the perturbation of modified QGPV, modified to consider the planetary vorticity advection by the isallobaric meridional wind in spherical geometry (Matsuno, 1970; Palmer, 1982); Z' is the curl of the horizontal GWD perturbation; $\boldsymbol{\nabla} \cdot \mathbf{F}$ is the divergence of Eliassen-Palm (EP) flux ($\mathbf{F}$), and the flux $\mathbf{F}$ is considered to be the wave-activity flux given by $\mathbf{F} = \mathbf{c}_g A$ in the QG framework, where $\mathbf{c}_g$ is the group velocity in the latitude-height domain.

In (1), the wave-activity density A and the modified QGPV perturbation $q'_{(M)}$ are given in spherical geometry (Palmer, 1982), respectively, as follows:

$$A = a \cos\phi \, \frac{1}{2} \rho_0 \frac{\overline{q'^2_{(M)}}}{\bar{q}_\phi / a}, \tag{2}$$

$$q'_{(M)} = \frac{v'_\lambda}{a \cos\phi} - \frac{f}{a \cos\phi} \left(\frac{u' \cos\phi}{f} \right)_\phi + \frac{f}{\rho_0} \left(\rho_0 \frac{\theta'}{\bar{\theta}_z} \right)_z, \tag{3}$$

where u and v are zonal and meridional wind components, respectively; λ is the longitude; f is the Coriolis parameter; θ is the potential temperature. The subscript λ and z mean the partial derivatives in longitude and vertical directions, respectively.

For understanding of amplification of PWs around the instability regions, the barotropic and baroclinic instability regions are determined by the negative sign of $\bar{q}_\phi$ (Andrews et al. 1987) given by:

$$\bar{q}_\phi = 2\Omega\cos\phi - \left[\frac{(\bar{u}\cos\phi)_\phi}{a\cos\phi}\right]_\phi - \frac{a}{\rho_0}\left(\frac{\rho_0 f^2}{N^2}\bar{u}_z\right)_z , \tag{4}$$

where Ω is the earth's rotation rate and N is the buoyancy frequency. The negative sign of $\bar{q}_\phi$ is a necessary condition of the barotropic and baroclinic instabilities. The second (with negative sign) and third (with negative sign) terms on the right-hand side of (4) represent the meridional and vertical curvatures of the zonal-mean zonal wind, respectively. If the second or third term is dominant, $\bar{q}_\phi$ can become negative, and the instabilities can take place.

The square of refractive index n^2 is used to analyze the propagation characteristics of PWs and depends on the mean QGPV gradient as follows:

$$n^2 = \frac{\bar{q}_\phi}{a(\bar{u}-c)} - \frac{s^2}{a^2\cos^2\phi} - \frac{f^2}{4N^2H^2}, \tag{5}$$

where c is the zonal phase speed of single PW (i.e., $c = 2\pi a\cos\phi/(s\tau)$; s is the zonal wavenumber, and τ is the wave period), and the constant scale height H is set equal to 7 km. The propagation of PWs is possible in regions of positive n^2. On the other hand, PWs can be reflected or be evanescent in the region where $n^2 < 0$ (Matsuno, 1970).

In order to analyze the wave propagation and wave activity for the selected dates for Q10DWs (or Q10DOs) found in MRs and model simulations, we use the EP flux as diagnostic tools, derived in the Transformed Eulerian-Mean framework for the spherical QG system (Palmer, 1982; Andrews et al., 1987). In the spherical geometry, the meridional [$F^{(\phi)}$] and vertical [$F^{(z)}$] components of the EP flux $\mathbf{F} \equiv [0, F^{(\phi)}, F^{(z)}]$ are given by

$$F^{(\phi)} = -\rho_0 a \cos\phi \overline{u'v'} \,, \qquad (6)$$

$$F^{(z)} = \rho_0 a \cos\phi\, f\, \overline{v'\theta'}/\bar{\theta}_z \,, \qquad (7)$$

Figure 4 shows the EP flux **F** and wave activity density normalized by $\rho_0\ a\cos\phi$ for Q10DWs in the EXP75. The propagation inhibition region ($n^2 < 0$) and the contours of zonal-mean zonal wind are overplotted. Thick green and black lines indicate the regions of $\bar{q}_\phi = 0$ and of critical lines for Q10DWs, respectively. The critical lines are plotted by computing the zonal phase speed (c) of Q10DW: $c = 2\pi a \cos\phi\ /(s\tau)$, where $s = 1$ and $\tau = 10$ day. The wave-activity density is shaded in blue and red depending on its sign [sgn(A)]. For the EP flux vector, $\mathbf{F}/\mathrm{sgn}(A)$ ($= \mathbf{c}_g|A|$), rather than **F** itself ($= \mathbf{c}_g A$), is plotted such that the EP flux can always be parallel to the local group velocity of Q10DWs regardless of the instability regions where $\bar{q}_\phi < 0$ and thus $A < 0$. For better illustration of the EP flux in the atmosphere where its density decreases exponentially with height, the meridional and vertical components of EP flux are scaled by $(p_s/p)^{0.85}[F^{(\phi)}/(a\pi), F^{(z)}/(3 \times 10^5)]$ (Edmon et al., 1980; Gan et al., 2018), where p_s and p are the surface and atmospheric pressures, respectively.

For Fig. 4, we select the four dates of (a) 30 April 2012, (b) 11 April 2013, (c) 6 April 2015, and (d) 29 October 2016 when the three criteria mentioned in Fig. 3 are satisfied (see yellow boxes in Fig. 3). That is, the normalized amplitudes of Q10DWs from both MRs and EXP75 are larger than its average, the correlation coefficient is larger than 0.6, and the hemispheric symmetry is found in the MLS results. The 30 April 2012 case (Fig. 4a) shows that the stratospheric jet is located around (40°S–60°S, 55 km) in the latitude-height domain and that there is a predominant branch of upward and equatorward Q10DW EP flux vectors across the center of the stratospheric jet. In the high-latitude mesosphere, there are two regions where both the large-scale instability ($\bar{q}_\phi < 0$) and evanescence ($n^2 < 0$) take place, and they are located in (55°S–65°S, 60–85 km) and (65°S–80°S, 70–110 km), respectively. Along the instability boundaries (green lines), large positive or negative Q10DW activities are found. Divergent EP flux vectors in the meridional direction are clearly seen around the instability region located at (53°S, 65–75 km), which implies the excitation of Q10DWs in association with the instability. In the region of MR observations (60°S–65°S, 85–100 km), substantially amplified Q10DW activity appears, and the equatorward Q10DW EP flux towards the MR sites is found over the amplified Q10DW activity.

Figure 4b demonstrates the case of 11 April 2013. One major branch of Q10DW EP flux vectors (Fig. 4b) originates from the stratospheric jet located at (55°S–60°S, 45–60 km). In the southern and upper side of the stratospheric jet, the instability and evanescent region extends from 45 km to 70 km height in the latitude of 50°S–75°S.

Above the instability region, distinct region of strong wave activity is found around (50°S–65°S, 65–90 km), and this region is partially overlapped by the MR observation region. Around this region, the Q10DW EP flux is directed downward and poleward inside of the instability region (within green line). The Q10DW EP flux is directed upward and equatorward outside and above the instability region. This diverging pattern of EP flux around the instability region also shows the possibility of the excitation of Q10DW in association with the instability.

For 6 April 2015 case (Fig. 4c), the structure of wave-activity density and instability regions are similar to the 30 April 2012 case (Fig. 4a). The instability and evanescent regions occur around (60°S–80°S, 70–100 km). Along the instability boundaries, there are strong positive and negative wave-activity densities, and this region of strong wave activities includes the MR observation region. Again, the divergence of Q10DW fluxes appears in the upper part of the instability region around (60°S–70°S, 80–100 km). The Q10DW propagates upward and equatorward outside of the instability region and downward inside of the instability region, as in the other dates shown in Figs. 4a and 4b. Unlike the other events, the propagation of Q10DW is poleward in the stratosphere (30–60 km altitude). This result is consistent with Qin et al. (2022). They reported that the meridional component of EP flux extends from the stratosphere in the NH across the equator to the SH stratosphere during the westerly phase of QBO in the middle stratosphere and during the westerly phase of the semi-annual oscillation in the upper stratosphere.

In 29 October 2016 case (Figure 4d), the center of stratospheric jet is located around (60°S–70°S, 20–30 km). Above the stratospheric jet, the eastward wind turns westward around the altitude of 60 km. Within the region of westward wind, the instability and evanescent regions are found. In addition, the critical lines exist inside the instability region. The overreflection or transmission process can take place near the critical lines as we mentioned. Notably, the significantly large positive and negative wave-activity density regions are found around (45°S–70°S, 60–90 km) near the instability boundaries, and these regions are partially overlapped by the MR observation region. This result suggests that the observed amplification of Q10DW may be attributed to the overreflection process. The EP flux of Q10DW predominantly propagates upward and equatorward away from the strong wave-activity region around (60°S, 60–70 km) with weak poleward propagation of Q10DW towards the instability region across the critical lines.

For all the cases shown in Fig. 4, the results indicate that a distinct strong wave-activity density region is located within the area observed by the MRs (around 60°S–70°S and 80–100 km in height), associated with the large-scale instability region. Considering the wave-activity density A is directly proportional and inverse proportional to the $\overline{q'^2}$ and $\bar{q}_\phi$, respectively, it can be thought that the small $\bar{q}_\phi$ contributes the large magnitude of A near the instability region. However, we confirm that the large $\overline{q'^2}$ is located around the instability region, leading to the overall large wave-activity density (not shown in here). In addition, the group velocity of the wave is given by $\mathbf{c}_g = \mathbf{F}/A$. For the selected cases (Fig. 4), the EP flux $\mathbf{F}$ in the MR observation region is relatively small, while the magnitude of A is comparatively large. This suggests a small group velocity in this region. These results agree with the study of

Thorncroft et al. (1993), which states that during the amplification of baroclinic waves, the group velocity tends to be small.

As previously mentioned, Song et al. (2020) proposed that the NCGWD can generate PWs. In addition, Forbes and Zhang (2015) suggested that the dissipation of gravity waves filtered by the Q10DW wind field can generate a secondary Q10DW by momentum deposition. In this regard, the both parameterized GWs and resolved GWs ($s \geq 20$) could also play a role in generating Q10DW. To verify the contribution of NCGWD, we analyze linearized disturbance QGPV equation (Andrews et al., 1987) for the 4 cases shown in Fig. 4. Our analysis shows that the contribution of both NCGWD and resolved GW for the Q10DW is negligible in the MLT region (see Fig. S3 in the Supplement).

These results indicate that the large amplitudes of Q10DW observed in the SH high-latitude region by the Davis and KSS MRs can originate from the high-latitude stratosphere-mesosphere region, where the barotropic/baroclinic instability or overreflection near the critical layer occur.

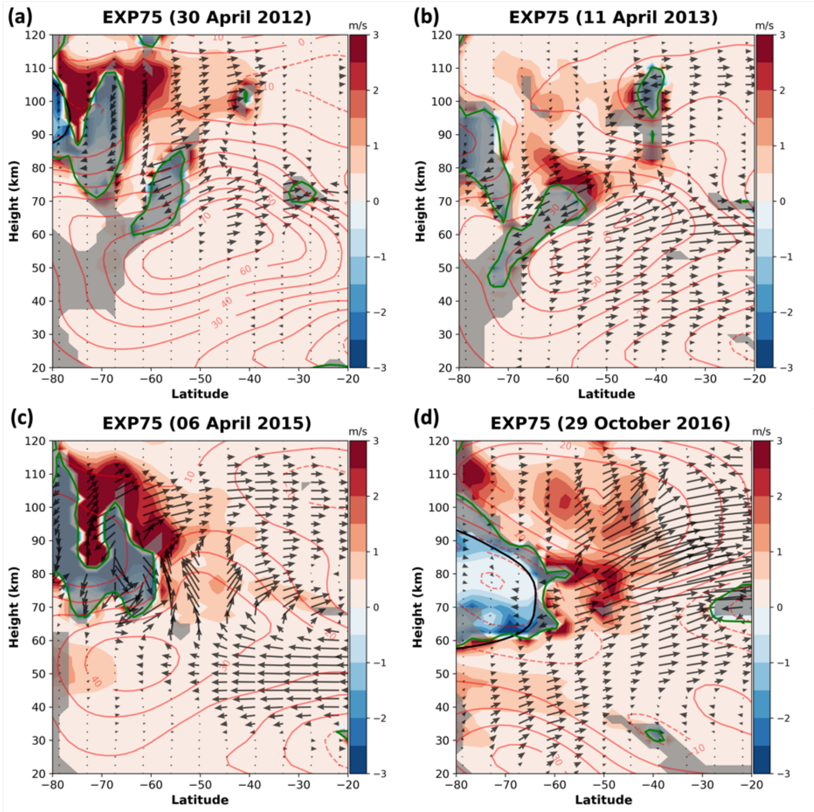

Figure 4. EP flux parallel to local group velocity [$\mathbf{F}/\mathrm{sgn}(A)$] and normalized wave activity density [$A\ (\rho_0 a \cos\phi)^{-1}$ given in the unit of m s^{-1}] for the Q10DWs in the EXP75 on (a) 30 April 2012, (b) 11 April 2013, (c) 6 April 2015, and (d) 29 October 2016. The activity density A is shaded in blue and red depending on its sign. The boundaries of the instability regions ($\bar{q}_\phi = 0$, green lines), the negative n^2 regions (grey shading), and the red contours for zonal-mean zonal wind are overplotted. For eastward (westward) zonal-mean zonal wind, contours are plotted in solid (dashed) lines, and contour interval is 10 m s^{-1}.

3.3 Comparison of Q10DO between SD-WACCM simulations

This section compares the Q10DOs around the mesospheric instability regions in the two SD-WACCM simulations (EXP75 and EXP60) for February and November.

February and November are chosen because the amplitudes of modeled Q10DOs are substantial. The magnitude of Q10DO in the EXP75 is generally smaller than that in the EXP60, which is more comparable to the MR and MLS observations in which both Q10DWs and Q10DOs are weak (see Figs. S1 and S2 in the Supplement). Note that more realistic meteorological fields are nudged throughout the mesosphere in the EXP75. In this section, comparison between EXP75 and EXP60 for February and November is carried out to reveal mechanisms behind weak Q10DOs in the EXP75.

Figure 5 demonstrates the properties of Q10DO and background atmospheric conditions (as shown in Fig. 4) for 5 February 2013 and 16 November 2016 when the Q10DO activity is found to be large in both simulations. The left and right panels of Fig. 5 are the results from the EXP75 and EXP60, respectively. In Fig. 5, it is clear that the strong wave-activity density for Q10DO arise in polar regions above the altitude of 70 km in the EXP60, and the magnitude of the EP fluxes in the EXP60 is much larger than that in EXP75. In addition, in 5 February 2013 for the EXP60 (Fig. 5b), a substantially strong wave-activity density region is located in the mid-latitude mesospheric region as well. Around the strong wave-activity regions in the polar upper mesosphere, it is seen that the EP fluxes of Q10DWs are divergent. In addition, the distinct wave-activity density of Q10DO regions in the EXP60 occur along the instability regions and critical lines around (50°S–70°S, 70–110 km) and (20°S–40°S, 65–80 km). On the other hand, the wave-activity density of Q10DO in the EXP75 (Fig. 5a and 5c) is located at relatively higher altitudes (80–100 km), and the strength of Q10DO EP flux and wave-activity density are weaker than EXP60. Moreover, the negative EP flux divergence (EPFD) is much larger in the EXP60 than in the EXP75 above the altitude of 80 km (not shown in here).

Our analysis reveals that the larger wave-activity density and EP fluxes in the EXP60 along the large-scale instability region in the polar upper mesosphere compared to the EXP75. This indicates that the stronger large-scale instability in the EXP60 can amplify Q10DO activities, which is consistent with the analysis result that the barotropic and baroclinic instabilities can be the major sources of the amplification of traveling PWs (Harvey et al., 2019).

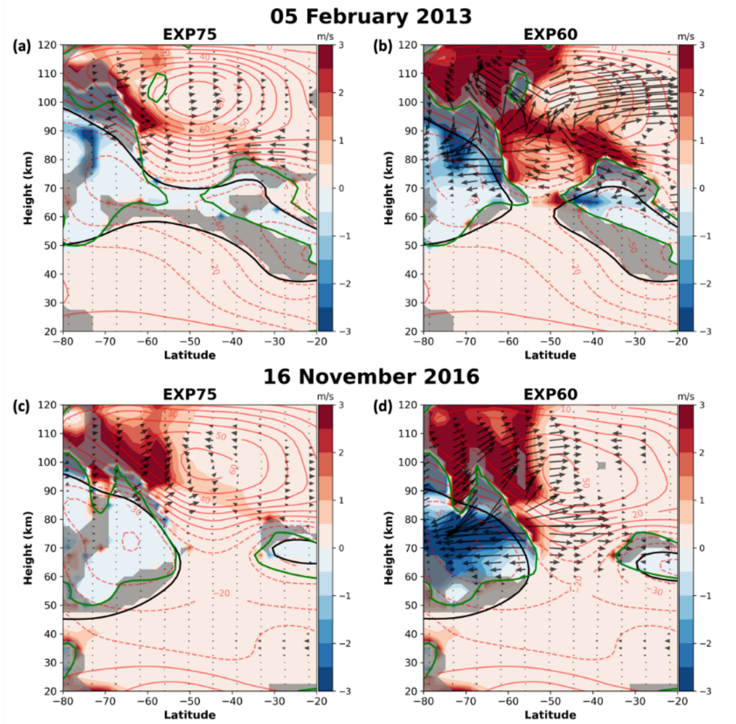

Figure 5. Same as Fig. 4 but for (a and b) 5 February 2013 and (c and d) 15 November 2016. The left and right columns represent the results from EXP75 and EXP60, respectively.

Figure 6 shows the $\bar{q}_{\phi}$ (normalized by Ω) for 5 February 2013 and 16 November 2016 from the EXP75 (blue), EXP60 (red), and MLS (black). The normalization makes $\bar{q}_{\phi}$ dimensionless. The $\bar{q}_{\phi}/\Omega$ from MLS is derived in the quasi-geostrophic framework

(Andrews et al., 1987) and it is included as a reference for validation. The $\bar{q}_\phi/\Omega$ is averaged between the latitudes of 65°S-80°S where the wave-activity density is strong and large negative $\bar{q}_\phi$ is found in Fig. 5. It is seen that the vertical profiles of $\bar{q}_\phi/\Omega$ from the EXP75 and MLS have somewhat small negative values and they are generally similar below the altitude of 75 km, although the difference gradually increase above the altitude of 75 km. On the other hand, large discrepancies are shown between EXP75 and EXP60 in the altitudes between 60–80 km. In the EXP60, $\bar{q}_\phi/\Omega$ has much larger negative values, which suggest the relatively stronger barotropic or baroclinic instability in the EXP60 and the amplification of the Q10DO in the mid-to-upper mesosphere in association with the stronger instability in the EXP60.

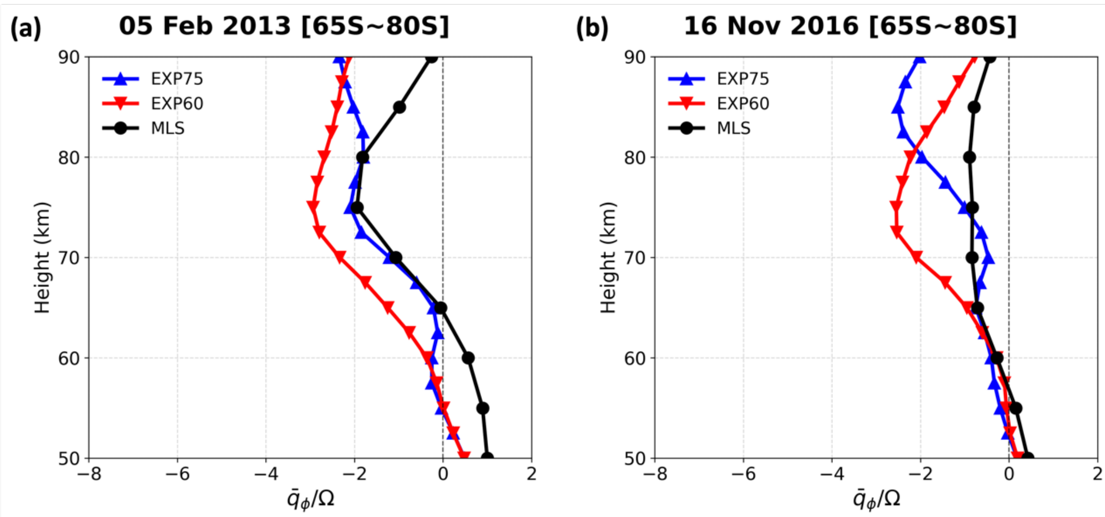

Figure 6. $\bar{q}_\phi$ (normalized by Ω) averaged over 65°S–85°S for (a) 5 February 2013 and (b) 16 November 2016 from the EXP75 (blue), EXP60 (red), and MLS (black).

The negative $\bar{q}_\phi$ can be induced by latitudinal and vertical curvatures of zonal-mean zonal wind that correspond to the second and third terms (with negative signs) in the right side of (4), respectively. Figure 7 shows the second (top panels) and third (bottom panels) terms, respectively, for 5 February 2013. The differences shown in Figs. 7c and 7f indicate that the larger negative $\bar{q}_{\phi}$ is located in the lower altitudes in the EXP60 than in EXP75, inducing the larger instability at 65–75 km in height around 70°S–80°S in the EXP60, which is consistent with Fig. 6. Note that the positive differences seen at about 65–75 km in the high-latitude regions in Figs. 7c and 7f mean the larger negative $\bar{q}_{\phi}$ in the EXP60. Also, it is clear that both vertical and horizontal shear contribute the stronger barotropic/baroclinic instability in the EXP60 in the mid-to-upper mesosphere, as shown in Figs. 7a-b and 7d-e. This analysis demonstrates the mesospheric dynamics specified by the MERRA-2 data up to the altitude of 75 km reduces the large-scale instability in the mid-to-upper mesosphere in the EXP75. This is consistent with Sassi et al. (2021) proposed the absence of specification of middle atmosphere dynamics induce the instability in summer mesospheric westward jet, leading large traveling PWs.

The wind structure in the MLT region is mainly driven by momentum deposition from PWs and GWs. Harvey et al. (2019) reported that GWs can change significantly the vertical shears, leading enhanced instability and larger traveling PWs in the mesospheric region based on the satellite observations and SD-WACCM simulations. GW forcing is one of the main factors to maintain the necessary conditions of barotropic/baroclinic instability in the modeled mesosphere (Sato et al., 2018). Therefore, in order to better understand the mechanisms underlying the discrepancies in zonal wind fields and the resulting instability in the model, it is important to examine the contribution of resolved wave forcing (EPFD) and GWD forcing on the zonal wind structure in the mesosphere.

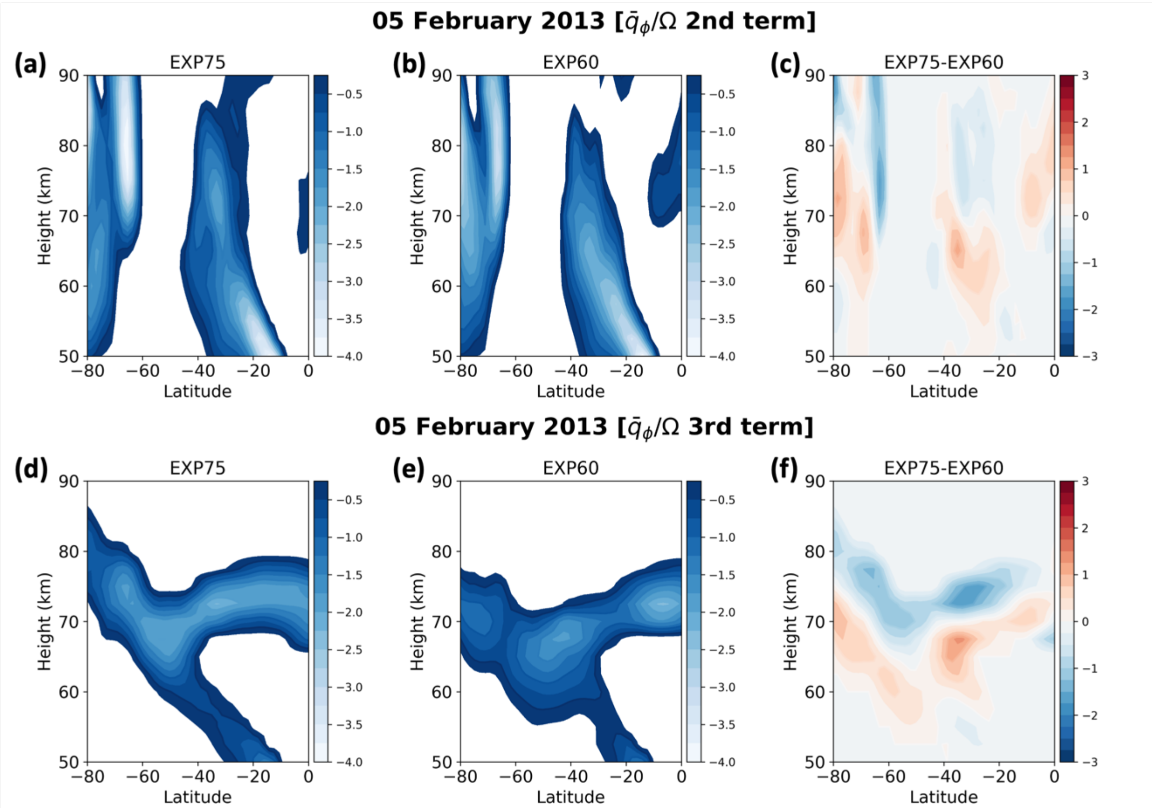

Figure 7. Contributions of (top) the meridional variation of the zonally-averaged mean flow and (bottom) its vertical variation to the instability condition (negative $\bar{q}_\phi$) shown in (2), respectively, for 5 February 2013. Panels in each column present the results from (a and d) the EXP75, (b and e) the EXP60, and (c and f) difference between EXP75 and EXP60, respectively. Only negative values are plotted except for two panels for difference.

Figure 8 shows the latitude-height distributions of zonal-mean zonal wind, zonal component of GWD and resolved wave forcing (EPFD) in 5 February 2013 for the EXP75, the EXP60, and the difference between EXP75 and EXP60 (EXP75–EXP60). The zonal-mean zonal wind, zonal component of GWD, and resolved wave forcing (EPFD) are calculated through the 21-day averaging (central date ± 10 days). For GWD, the orographic and nonorographic values are added. In Figs. 8a–b, zero-wind lines are located around 80 km height in the SH mid-latitude region, indicating the reversal of the zonal-mean zonal wind due to the eastward momentum forcing from the GWs and resolved waves. It is clear that the zero-wind line in the EXP60 is located at lower altitudes by about 5 km compared to the EXP75, which means that eastward GWD and eastward EPFD from the EXP60 can be larger below the altitude of ~80 km than that from EXP75. Indeed, the difference field between EXP75 and EXP60 for GWD (Fig. 8f) shows that the eastward GWD from the EXP60 is larger around (60°S, 70 km) than that from EXP75 as indicated by the negative difference field in those regions. In addition, the resolved wave forcing (EP flux divergence) is more eastward above the altitude of 70 km in the mid-to-high latitude regions in the EXP60 than in the EXP75. This result indicates that the eastward resolved wave forcing also contributes more in the mid-to-upper mesosphere in the EXP60, resulting in the zonal-mean zonal wind reversal (westward to eastward wind) in the lower altitude in the EXP60, as shown around 60°S in Fig. 8b.

As mentioned before, the amplification or modulation of westward-propagating PWs with zonal wavenumber 1 and a quasi-10-day period due to NCGWD and resolved GW is negligible (Fig. S3 in Supplement), indicating that the amplification of Q10DW or Q10DO is mainly related to the baroclinic/barotropic instability. The stronger instability in the EXP60 around the altitude of 70 km indicates that WACCM simulates a large meridional and vertical variation of zonal winds compared to the observations in the mid-to-upper mesosphere, which is likely due to the stronger eastward GWD and eastward EPFD forcing near 70 km altitude in the EXP60, as shown in Fig. 8. Cohen et al. (2013) reported that parameterized GWs can generate instability that can generate resolved waves of which forcing (i.e., EPFD) can compensate GWD. Our results show that the increased eastward GWD at 70 km altitude generates instability and it leads more Q10DO. The EPFD in the EXP60 gives the more eastward forcing above 70 km enhancing the wind reversal in the mid-to-high latitudes. However, comparison of Figs. 8f and 8i indicates that the structures of GWD and EPFD are roughly 90°–180° shifted in the vertical direction, approximately consistent with the compensation between GWD and EPFD. Raising the nudging altitude of MERRA-2 reanalysis data to 75 km from 60 km reduces the instability in the mid-to-upper mesosphere, leading to decreased the Q10DO activity in the EXP75. Therefore, we suggest that strong eastward GWD in the mid-to-upper mesosphere in summer need to be alleviated, which can generate more instability in the SH high-latitude mesosphere region that can lead to discrepancy from observations.

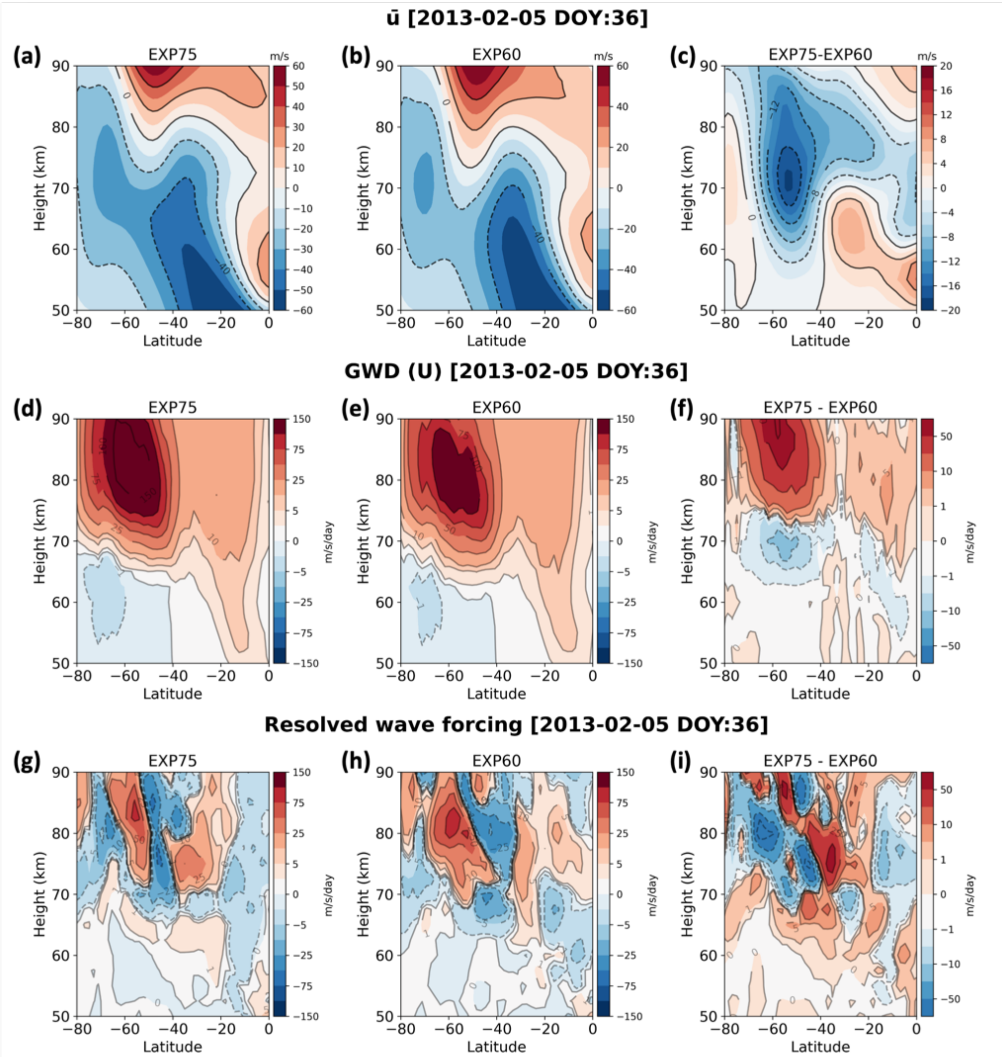

Figure 8. Latitude-height distributions of (a–c) zonal-mean zonal wind, (d–f) zonal component of GWD and (g–i) resolved wave forcing (EP flux divergence) in 5 February 2013 for (left) the EXP75, (middle) the EXP60, and (right) difference between EXP75 and EXP60 (EXP75–EXP60).

4. Conclusions

In this paper, the seasonal variation and the amplification mechanism of Q10DW during 2012–2016 in the SH high-latitude regions are investigated using two MRs located in Antarctica, and SD-WACCM simulations. Using the phase difference of meridional winds measured by two MRs, we extract westward-propagating Q10DW with zonal wavenumber 1. The seasonal variation of the observed Q10DW shows that the amplitude is strong during equinoxes, which is consistent with previous studies. In addition, our study shows the Q10DWs from the MLS appear to be consistently overestimated compared to those from MRs. These discrepancies can be due to both errors in estimating winds from the MLS and uncertainties in results obtained from two MR stations alone. Further investigation is required for more reliable estimation of the amplitude and phase of Q10DWs from observations.

In order to elucidate the amplification mechanism of Q10DW observed by MRs during equinoxes, two SD-WACCM experiments are carried out using the MERRA-2 reanalysis data from surface to ~60 km (EXP60) and ~75 km (EXP75), respectively. The temporal variation of the averaged amplitude of Q10DW in the EXP75 during 2012–2016 is in better agreement with the MR observations. Meanwhile, the amplitude of Q10DW in the EXP60 is excessively large compared with the observations. Based on the analysis of meridional gradient of the QGPV and wave-activity density, the Q10DW observed in the SH high-latitude region by the MRs originated in situ around the high-latitude stratosphere-mesosphere region, where the large-scale instability or overreflection near the critical lines occur. The unrealistically large magnitude of Q10DO (quasi-10-day-like oscillations without satisfying the hemispheric symmetry unlike Q10DW) is simulated in the EXP60 during February and November. In order to understand mechanisms of the large amplitude of Q10DO in the EXP60 during the SH summer, we compare the meridional gradient of QGPV from EXP75 and EXP60. The results show that specified dynamics with MERRA-2 reanalysis data mitigate the meridional and vertical variation of zonal winds in the polar mid-to-upper mesosphere in the EXP75, resulting in reduction in the large-scale instability. On the other hand, the large amplitude of Q10DO in the EXP60 is attributed to the large-scale instability related to the GWD and partially to the EPFD in the polar mid-to-upper mesosphere.

The polar mesospheric GWD can lead to strong large-scale instability in the SH high-latitude mesosphere and unrealistically large amplitude of Q10DO in summer. The present study on the amplification mechanism of Q10DW during equinoxes, and the unrealistic Q10DO amplitude in summer provide potential importance of large-scale instability, which can be to a substantial degree caused by parameterized GWD, during summer in the polar mesosphere for numerical models. In this paper, we focus on the Q10DW relating to the large-scale instability and polar mesospheric GWD, but other normal modes of PW will be considered for future studies.

Results of SD-WACCM may depend on the extra damping above the middle mesosphere in the GEOS-6 model (Fujiwara et al., 2017) used to produce the MERRA-2 data. The damping may have harmful effects on the results for the upper mesosphere in the EXP75, where the dynamics is still specified above the middle mesosphere using the MERRA-2, but comparison with observations shows that the zonal asymmetric structure of mesospheric temperature in the EXP75 is reasonable for the time periods of our interest (Fig. S5). However, the activity and variability of mesospheric PWs in the

MERRA-2 and SD-WACCM need to be further examined for the longer time periods and evaluated against other observations to support the reliability of results obtained in this study, which should be a topic of continuing research.

Code and Data availability

The source code of Community Earth System Model 2 (CESM2) developed at the National Center for Atmospheric Research (NCAR) is available at https://www.cesm.ucar.edu/models/cesm2. The atmospheric forcing data for specified dynamics are available from NCAR Research Data Archive (RDA) at https://rda.ucar.edu.

The Davis station meteor radar data are available from the Australian Antarctic Data Centre at https://data.aad.gov.au/metadata/records/Davis_33MHz_Meteor_Radar. The King Sejong Station meteor radar data are available from Korea Polar Data Center (KPDC) at https://kpdc.kopri.re.kr. The GPH data from the MLS onboard the NASA's EOS Aura satellite are available from Goddard Earth Science Data and Information Services Center (GES DISC) at https://daac.gsfc.nasa.gov.

Author contributions

WL and ISS designed the study, together with YHK, and wrote the manuscript. WL performed the analysis of the observational (MR and satellite) data in collaboration with ISS. ISS designed the SD-WACCM experiments. WL and ISS carried out the SD-WACCM experiments, ISS and BGS aided in interpreting the analysis of action conservation equation for Rossby waves. All authors discussed the results and contributed to the final manuscript.

Competing interests

The authors declare that they have no conflict of interest.

Acknowledgements

This research was supported by the Korea Astronomy and Space Science Institute under the R&D programs (Project No. 2023-1-850-07 and 2024-1-850-02) supervised by the Ministry of Science and ICT. The second author (In-Sun Song) was supported by the Yonsei University Research Funds of 2022 and 2023 (2022-22-0098 and 2023-22-0095).

References

Andrews, D. G., Holton, J. R., and Leovy, C. B.: Middle Atmosphere Dynamics, Elsevier, New York, USA, 489 pp., 1987.

Beres, J. H., Garcia, R. R., Boville, B. A., and Sassi, F.: Implementation of a gravity wave source spectrum parameterization dependent on the properties of convection in the Whole Atmosphere Community Climate Model (WACCM), J. Geophys. Res.-Atmos., 110, https://doi.org/10.1029/2004jd005504, 2005.

Brakebusch, M., Randall, C. E., Kinnison, D. E., Tilmes, S., Santee, M. L., and Manney, G. L.: Evaluation of Whole Atmosphere Community Climate Model simulations of ozone during Arctic winter 2004–2005, J. Geophys. Res.-Atmos., 118, 2673–2688, https://doi.org/10.1002/jgrd.50226, 2013.

Chandran, A., Garcia, R. R., Collins, R. L., and Chang, L. C.: Secondary planetary waves in the middle and upper atmosphere following the stratospheric sudden warming event of January 2012, Geophys. Res. Lett., 40, 1861–1867, https://doi.org/10.1002/grl.50373, 2013.

Charron, M. and Manzini, E.: Gravity waves from fronts: Parameterization and middle atmosphere response in a general circulation model, J. Atmos. Sci., 59, 923–941, https://doi.org/10.1175/1520-0469(2002)059<;0923:gwffpa>2.0.co;2, 2002.

Cohen, N. Y., Gerber, E. P. and Bühler, O.: Compensation between resolved and unresolved wave driving in the stratosphere: Implications for downward control, J. Atmos. Sci., 70, 3780–3798, https://doi.org/10.1175/jas-d-12-0346.1, 2013.

Danabasoglu, G., Lamarque, J. -F., Bacmeister, J., Bailey, D. A., DuVivier, A. K., Edwards, J., Emmons, L. K., Fasullo, J., Garcia, R., Gettelman, A., Hannay, C., Holland, M. M., Large, W. G., Lauritzen, P. H., Lawrence, D. M., Lenaerts, J. T. M., Lindsay, K., Lipscomb, W. H., Mills, M. J., Neale, R., Oleson, K. W., Otto-Bliesner, B., Phillips, A. S., Sacks, W., Tilmes, S., Kampenhout, L., Vertenstein, M., Bertini, A., Dennis, J., Deser, C., Fischer, C., Fox-Kemper, B., Kay, J. E., Kinnison, D., Kushner, P. J., Larson, V. E., Long, M. C., Mickelson, S., Moore, J. K., Nienhouse, E., Polvani, L., Rasch, P. J., and Strand, W. G.: The Community Earth System Model Version 2 (CESM2), J. Adv. Model. Earth. Sy., 12, https://doi.org/10.1029/2019ms001916, 2020.

Day, K. A. and Mitchell, N. J.: The 5-day wave in the Arctic and Antarctic mesosphere and lower thermosphere, J. Geophys. Res.-Atmos., 1984–2012, 115, https://doi.org/10.1029/2009jd012545, 2010.

Edmon, H. J., Hoskins, B. J., and McIntyre, M. E.: Eliassen-Palm cross sections for the troposphere, J. Atmos. Sci., 37, 2600–2616, https://doi.org/10.1175/1520-0469(1980)037<;2600:epcsft>2.0.co;2, 1980.

Egito, F., Takahashi, H., and Miyoshi, Y.: Effects of the planetary waves on the MLT airglow, Ann. Geophys., 35, 1023–1032, https://doi.org/10.5194/angeo-35-1023-2017, 2017.

Eswaraiah, S., Kim, Y. H., Hong, J., Kim, J.-H., Ratnam, M. V., Chandran, A., Rao, S. V. B., and Riggin, D.: Mesospheric signatures observed during 2010 minor stratospheric warming at King Sejong Station (62°S, 59°W), J. Atmos. Sol-Terr. Phy., 140, 55–64, https://doi.org/10.1016/j.jastp.2016.02.007, 2016.

Eswaraiah, S., Ratnam, M. V., Kim, Y. H., Kumar, K. N., Chalapathi, G. V., Ramanajaneyulu, L., Lee, J., Prasanth, P. V., Thyagarajan, K., and Rao, S. V. B.: Advanced meteor radar observations of mesospheric dynamics during 2017 minor SSW over the tropical region, Adv. Space. Res., 64, 1940–1947, https://doi.org/10.1016/j.asr.2019.05.039, 2019.

Eyring, Veronika, et al.: Overview of IGAC/SPARC Chemistry-Climate Model Initiative (CCMI) community simulations in support of upcoming ozone and climate assessments, SPARC newsletter, 40, 48–66, https://oceanrep.geomar.de/id/eprint/20227, 2013.

Forbes, J. M. and Zhang, X.: Quasi-10-day wave in the atmosphere, J. Geophys. Res.-Atmos., 120, 11,079–11,089, https://doi.org/10.1002/2015jd023327, 2015.

Forbes, J. M. and Zhang, X.: The quasi-6 day wave and its interactions with solar tides, J. Geophys. Res.-Space, 122, 4764–4776, https://doi.org/10.1002/2017ja023954, 2017.

Forbes, J. M., Hagan, M. E., Miyahara, S., Vial, F., Manson, A. H., Meek, C. E., and Portnyagin, Y. I.: Quasi 16-day oscillation in the mesosphere and lower thermosphere, J. Geophys. Res.-Atmos., 100, 9149–9163, https://doi.org/10.1029/94jd02157, 1995.

Forbes, J. M., Zhang, X., Heelis, R., Stoneback, R., Englert, C. R., Harlander, J. M., Harding, B. J., Marr, K. D., Makela, J. J., and Immel, T. J.: Atmosphere-Ionosphere (A-I) coupling as viewed by ICON: Day-to-day variability due to planetary wave (PW)-tide interactions, J. Geophys. Res.-Space, 126, https://doi.org/10.1029/2020ja028927, 2021.

Fujiwara, M., Wright, J. S., Manney, G. L., Gray, L. J., Anstey, J., Birner, T., Davis, S., Gerber, E. P., Harvey, V. L., Hegglin, M. I., Homeyer, C. R., Knox, J. A., Krüger, K., Lambert, A., Long, C. S., Martineau, P., Molod, A., Monge-Sanz, B. M., Santee, M. L., Tegtmeier, S., Chabrillat, S., Tan, D. G. H., Jackson, D. R., Polavarapu, S., Compo, G. P., Dragani, R., Ebisuzaki, W., Harada, Y., Kobayashi, C., McCarty, W., Onogi, K., Pawson, S., Simmons, A., Wargan, K., Whitaker, J. S., and Zou, C.-Z.: Introduction to the SPARC Reanalysis Intercomparison Project (S-RIP) and overview of the reanalysis systems, Atmos. Chem. Phys., 17, 1417–1452, https://doi.org/10.5194/acp-17-1417-2017, 2017.

Gan, Q., Oberheide, J., and Pedatella, N. M.: Sources, sinks, and propagation characteristics of the quasi 6-day wave and its impact on the residual mean circulation, J. Geophys. Res.-Atmos., 123, 9152–9170, https://doi.org/10.1029/2018jd028553, 2018.

Gelaro, R., McCarty, W., Suárez, M. J., Todling, R., Molod, A., Takacs, L., Randles, C. A., Darmenov, A., Bosilovich, M. G., Reichle, R., Wargan, K., Coy, L., Cullather, R., Draper, C., Akella, S., Buchard, V., Conaty, A., Silva, A. M. da, Gu, W., Kim, G.-K., Koster, R., Lucchesi, R., Merkova, D., Nielsen, J. E., Partyka, G., Pawson, S., Putman, W., Rienecker, M., Schubert, S. D., Sienkiewicz, M., and Zhao, B.: The Modern-Era Retrospective Analysis for Research and Applications, Version 2 (MERRA-2), J. Climate, 30, 5419–5454, https://doi.org/10.1175/jcli-d-16-0758.1, 2017.

Goncharenko, L. P., Harvey, V. L., Greer, K. R., Zhang, S. -R., and Coster, A. J.: Longitudinally dependent low-latitude ionospheric disturbances linked to the Antarctic sudden stratospheric warming of September 2019, J. Geophys. Res.-Space, 125, https://doi.org/10.1029/2020ja028199, 2020.

Harvey, V. L., Knox, J. A., France, J. A., Fujiwara, M., Gray, L., Hirooka, T., Hitchcock, P., Hitchman, M., Kawatani, Y., Manney, G. L., McCormack, J., Orsolini, Y., Sakazaki, T., and Tomikawa, Y.: Chapter 11: Upper Stratosphere and Lower Mesosphere, SPARC Reanalysis Intercomparison Project (S-RIP) Final Report, edited by: Fujiwara, M., Manney, G. L., Gray, L. J., and Wright, J. S., SPARC Report No. 10, WCRP-6/2021, SPARC, DLR-IPA, Oberpfaffenhofen, Germany, https://doi.org/10.17874/800dee57d13, 2021.

Harvey, V. L., Randall, C. E., Becker, E., Smith, A. K., Bardeen, C. G., France, J. A., and Goncharenko, L. P.: Evaluation of the mesospheric polar vortices in WACCM, J. Geophys. Res.-Atmos., 124, 10626–10645, https://doi.org/10.1029/2019jd030727, 2019.

He, M., Chau, J. L., Stober, G., Li, G., Ning, B., and Hoffmann, P.: Relations between semidiurnal tidal variants through diagnosing the zonal wavenumber using a phase differencing technique based on two ground-based detectors, J. Geophys. Res.-Atmos., 123, 4015–4026, https://doi.org/10.1002/2018jd028400, 2018.

He, M., Chau, J. L., Forbes, J. M., Thorsen, D., Li, G., Siddiqui, T. A., Yamazaki, Y., and Hocking, W. K.: Quasi-10-day wave and semidiurnal tide nonlinear interactions during the Southern Hemispheric SSW 2019 observed in the Northern Hemispheric mesosphere, Geophys. Res. Lett., 47, https://doi.org/10.1029/2020gl091453, 2020a.

He, M., Yamazaki, Y., Hoffmann, P., Hall, C. M., Tsutsumi, M., Li, G., and Chau, J. L.: Zonal wave number diagnosis of Rossby wave-like oscillations using paired ground-based radars, J. Geophys. Res.-Atmos., 125, https://doi.org/10.1029/2019jd031599, 2020b.

Hirooka, T.: Normal mode Rossby waves as revealed by UARS/ISAMS observations, J. Atmos. Sci., 57, 1277–1285, https://doi.org/10.1175/1520-0469(2000)057<1277:NMRWAR>2.0.CO;2, 2000.

Holdsworth, D. A., Murphy, D. J., Reid, I. M., and Morris, R. J.: Antarctic meteor observations using the Davis MST and meteor radars, Adv. Space Res., 42, 143–154, https://doi.org/10.1016/j.asr.2007.02.037, 2008.

Huang, C., Zhang, S., Chen, G., Zhang, S., and Huang, K.: Planetary wave characteristics in the lower atmosphere over Xianghe (117.00°E, 39.77°N), China, revealed by the Beijing MST radar and MERRA data, J. Geophys. Res.-Atmos., 122, 9745–9758, https://doi.org/10.1002/2017jd027029, 2017.

Huang, C., Li, W., Zhang, S., Chen, G., Huang, K., and Gong, Y.: Investigation of dominant traveling 10-day wave components using long-term MERRA-2 database, Earth Planets Space, 73, 85, https://doi.org/10.1186/s40623-021-01410-7, 2021.

Huang, Y.-Y., Cui, J., Li, H.-J., and Li, C.-Y.: Inter-annual variations of 6.5-day planetary waves and their relations with QBO, Earth Planet. Phys., 6, 135–148, https://doi.org/10.26464/epp2022005, 2022.

Jablonowski, C. and Williamson, D. L.: Numerical techniques for global atmospheric models, Lect. Notes Comput. Sci. Eng., 381–493, https://doi.org/10.1007/978-3-642-11640-7_13, 2011.

Lee, W., Song, I., Kim, J., Kim, Y. H., Jeong, S., Eswaraiah, S., and Murphy, D. J.: The observation and SD-WACCM simulation of planetary wave activity in the middle atmosphere during the 2019 Southern Hemispheric sudden stratospheric warming, J. Geophys. Res.-Space, 126, https://doi.org/10.1029/2020ja029094, 2021.

Lee, W., Lee, C., Kim, J., Kam, H., and Kim, Y. H.: A modeling analysis of the apparent linear relation between mesospheric temperatures and meteor height distributions measured by a meteor radar, J. Geophys. Res.-Space, 127, https://doi.org/10.1029/2021ja029812, 2022.

Lee, W., Kim, Y. H., Lee, C., and Wu, Q.: First comparison of mesospheric winds measured with a Fabry-Perot interferometer and meteor radar at the King Sejong Station (62.2°S, 58.8°W), J. Astron. Space Sci., https://doi.org/10.5140/JASS.2018.35.4.235, 2018

Li, W., Huang, C., and Zhang, S.: Global characteristics of the westward-propagating quasi-16-day wave with zonal wavenumber 1 and the connection with the 2012/2013 SSW revealed by ERA-Interim, Earth Planets Space, 73, 113, https://doi.org/10.1186/s40623-021-01431-2, 2021.

Lindzen, R. S., Farrell, B., and Tung, K.-K.: The concept of wave overreflection and its application to baroclinic instability, J. Atmos. Sci., 37, 44–63, https://doi.org/10.1175/1520-0469(1980)037<;0044:tcowoa>2.0.co;2, 1980.

Liu, G., Janches, D., Lieberman, R. S., Moffat-Griffin, T., Mitchell, N. J., Kim, J., and Lee, C.: Wind variations in the mesosphere and lower thermosphere near 60°S latitude during the 2019 Antarctic sudden stratospheric warming, J. Geophys. Res.-Space, 126, https://doi.org/10.1029/2020ja028909, 2021.

Liu, G., Janches, D., Ma, J., Lieberman, R. S., Stober, G., Moffat-Griffin, T., Mitchell, N. J., Kim, J., Lee, C., and Murphy, D. J.: Mesosphere and lower thermosphere winds and tidal variations during the 2019 Antarctic sudden stratospheric warming, J. Geophys. Res.-Space, 127, https://doi.org/10.1029/2021ja030177, 2022.

Luo, J., Gong, Y., Ma, Z., Zhang, S., Zhou, Q., Huang, C., Huang, K., Yu, Y., and Li, G.: Study of the quasi 10-day waves in the MLT region during the 2018 February SSW by a meteor radar chain, J. Geophys. Res.-Space, 126, https://doi.org/10.1029/2020ja028367, 2021.

Ma, Z., Gong, Y., Zhang, S., Xiao, Q., Xue, J., Huang, C., and Huang, K.: Understanding the excitation of quasi-6-day waves in both hemispheres during the September 2019 Antarctic SSW, J. Geophys. Res.-Atmos., 127, https://doi.org/10.1029/2021jd035984, 2022.

Marsh, D. R., Mills, M. J., Kinnison, D. E., Lamarque, J.-F., Calvo, N., and Polvani, L. M.: Climate change from 1850 to 2005 simulated in CESM1(WACCM), J. Climate, 26, 130509150556003, https://doi.org/10.1175/jcli-d-12-00558.1, 2013.

Matsuno, T.: Vertical propagation of stationary planetary waves in the winter Northern Hemisphere, J. Atmos. Sci., 27, 871–883, https://doi.org/10.1175/1520-0469(1970)027<;0871:vpospw>2.0.co;2, 1970.

Matthias, V. and Ern, M.: On the origin of the mesospheric quasi-stationary planetary waves in the unusual Arctic winter 2015/2016, Atmos. Chem. Phys., 18, 4803–4815, https://doi.org/10.5194/acp-18-4803-2018, 2018.

Matthias, V., Hoffmann, P., Rapp, M., and Baumgarten, G.: Composite analysis of the temporal development of waves in the polar MLT region during stratospheric warmings, J. Atmos. Sol.-Terr. Phys., 90, 86–96, https://doi.org/10.1016/j.jastp.2012.04.004, 2012.

McCormack, J. P., Harvey, V. L., Randall, C. E., Pedatella, N., Koshin, D., Sato, K., Coy, L., Watanabe, S., Sassi, F., and Holt, L. A.: Intercomparison of middle atmospheric meteorological analyses for the Northern Hemisphere winter 2009–2010, Atmos. Chem. Phys., 21, 17577–17605, https://doi.org/10.5194/acp-21-17577-2021, 2021.

McFarlane, N. A.: The effect of orographically excited gravity wave drag on the general circulation of the lower stratosphere and troposphere, J. Atmos. Sci., 44, 1775–1800, https://doi.org/10.1175/1520-0469(1987)044<;1775:teooeg>2.0.co;2, 1987.

Meyer, C. K. and Forbes, J. M.: A 6.5-day westward propagating planetary wave: Origin and characteristics, J. Geophys. Res.-Atmos., 102, 26173–26178, https://doi.org/10.1029/97jd01464, 1997.

Mitra, G., Guharay, A., Batista, P. P., and Buriti, R. A.: Impact of the September 2019 minor sudden stratospheric warming on the low-latitude middle atmospheric planetary wave dynamics, J. Geophys. Res.-Atmos., 127, https://doi.org/10.1029/2021jd035538, 2022.

Palmer, T. N.: Properties of the Eliassen-Palm flux for planetary scale motions, J. Atmos. Sci., 39, 992–997, https://doi.org/10.1175/1520-0469(1982)039<;0992:potepf>2.0.co, 1982.

Qin, Y., Gu, S., Dou, X., Gong, Y., Chen, G., Zhang, S., and Wu, Q.: Climatology of the quasi-6-day wave in the mesopause region and its modulations on total electron content during 2003–2017, J. Geophys. Res.-Space, 124, 573–583, https://doi.org/10.1029/2018ja025981, 2019.

Qin, Y., Gu, S., Dou, X., Teng, C., Yang, Z., and Sun, R.: Southern Hemisphere response to the secondary planetary waves generated during the Arctic sudden stratospheric final warmings: Influence of the quasi-biennial oscillation, J. Geophys. Res.-Atmos., 127, https://doi.org/10.1029/2022jd037730, 2022.

Qin, Y., Gu, S., Teng, C., Dou, X., Yu, Y., and Li, N.: Comprehensive study of the climatology of the quasi-6-day wave in the MLT region based on Aura/MLS observations and SD-WACCM-X simulations, J. Geophys. Res.-Space, 126, https://doi.org/10.1029/2020ja028454, 2021.

Reynolds, R. W., Rayner, N. A., Smith, T. M., Stokes, D. C., and Wang, W.: An improved in situ and satellite SST analysis for climate, J. Climate, 15, 1609–1625, https://doi.org/10.1175/1520-0442(2002)015<;1609:aiisas>2.0.co;2, 2002.

Rhodes, C. T., Limpasuvan, V., and Orsolini, Y. J.: Eastward-propagating planetary waves prior to the January 2009 sudden stratospheric warming, J. Geophys. Res.-Atmos., 126, https://doi.org/10.1029/2020jd033696, 2021.

Richter, J. H., Sassi, F., and Garcia, R. R.: Toward a physically based gravity wave source parameterization in a general circulation model, J. Atmos. Sci., 67, 136–156, https://doi.org/10.1175/2009jas3112.1, 2010.

Salby, M. L.: Rossby normal modes in nonuniform background configurations. Part I: Simple fields, J. Atmos. Sci., 38, 1803–1826, https://doi.org/10.1175/1520-0469(1981)038<;1803:rnminb>2.0.co;2, 1981a.

Salby, M. L.: Rossby normal modes in nonuniform background configurations. Part II. Equinox and solstice conditions, J. Atmos. Sci., 38, 1827–1840, https://doi.org/10.1175/1520-0469(1981)038<;1827:rnminb>2.0.co;2, 1981b.

Salby, M. L.: Survey of planetary-scale traveling waves: The state of theory and observations, Rev. Geophys., 22, 209–236, https://doi.org/10.1029/rg022i002p00209, 1984.

Sassi, F., McCormack, J. P., Tate, J. L., Kuhl, D. D., and Baker, N. L.: Assessing the impact of middle atmosphere observations on day-to-day variability in lower thermospheric winds using WACCM-X, J. Atmos. Sol.-Terr. Phys., 212, 105486, https://doi.org/10.1016/j.jastp.2020.105486, 2021.

Sassi, F. and Liu, H.-L.: Westward traveling planetary wave events in the lower thermosphere during solar minimum conditions simulated by SD-WACCM-X, J. Atmos. Sol.-Terr. Phys., 119, 11–26, https://doi.org/10.1016/j.jastp.2014.06.009, 2014.

Sato, K., Yasui, R., and Miyoshi, Y.: The momentum budget in the stratosphere, mesosphere, and lower thermosphere. Part I: Contributions of different wave types and in situ generation of Rossby waves, J. Atmos. Sci., 75, 3613–3633, https://doi.org/10.1175/jas-d-17-0336.1, 2018.

Schwartz, M. J., Lambert, A., Manney, G. L., Read, W. G., Livesey, N. J., Froidevaux, L., Ao, C. O., Bernath, P. F., Boone, C. D., Cofield, R. E., Daffer, W. H., Drouin, B. J., Fetzer, E. J., Fuller, R. A., Jarnot, R. F., Jiang, J. H., Jiang, Y. B., Knosp, B. W., Krüger, K., Li, J. -L. F., Mlynczak, M. G., Pawson, S., Russell, J. M., Santee, M. L., Snyder, W. V., Stek, P. C., Thurstans, R. P., Tompkins, A. M., Wagner, P. A., Walker, K. A., Waters, J. W., and Wu, D. L.: Validation of the Aura Microwave Limb Sounder temperature and geopotential height measurements, J. Geophys. Res.-Atmos. 1984 2012, 113, https://doi.org/10.1029/2007jd008783, 2008.

Song, B.-G., Chun, H.-Y., and Song, I.-S.: Role of gravity waves in a vortex-split sudden stratospheric warming in January 2009, J. Atmos. Sci., 77, 3321–3342, https://doi.org/10.1175/jas-d-20-0039.1, 2020.

Thorncroft, C. D., Hoskins, B. J., and McIntyre, M. E.: Two paradigms of baroclinic-wave life-cycle behaviour, Q. J. Roy. Meteor. Soc., 119, 17–55, https://doi.org/10.1002/qj.49711950903, 1993.

Torrence, C. and Compo, G. P.: A practical guide to wavelet analysis, B. Am. Meteorol. Soc., 79, 61–78, https://doi.org/10.1175/1520-0477(1998)079<0061:apgtwa>2.0.co;2, 1998.

Walker, S. N., Sahraoui, F., Balikhin, M. A., Belmont, G., Pinçon, J. L., Rezeau, L., Alleyne, H., Cornilleau-Wehrlin, N., and André, M.: A comparison of wave mode identification techniques, Ann. Geophys., 22, 3021–3032, https://doi.org/10.5194/angeo-22-3021-2004, 2004.

Wang, J. C., Palo, S. E., Forbes, J. M., Marino, J., Moffat-Griffin, T., and Mitchell, N. J.: Unusual Quasi 10-Day Planetary wave activity and the ionospheric response during the 2019 Southern Hemisphere sudden Stratospheric Warming, J. Geophys. Res.-Space, 126, https://doi.org/10.1029/2021ja029286, 2021.

Yamazaki, Y. and Matthias, V.: Large-amplitude quasi-10-day waves in the middle atmosphere during final warmings, J. Geophys. Res.-Atmos., 124, 9874–9892, https://doi.org/10.1029/2019jd030634, 2019.

Yin, S., Ma, Z., Gong, Y., Zhang, S., and Li, G.: Response of quasi-10-day waves in the MLT region to the sudden stratospheric warming in March 2020, Adv. Space Res., 71, 298–305, https://doi.org/10.1016/j.asr.2022.10.054, 2023.